Applied Surface Science 513 (2020) 145858

Contents lists available at ScienceDirect

Applied Surface Science

journal homepage: www.elsevier.com/locate/apsusc

Full Length Article

Vanadium-Doped $SrTiO_3$ Nanocubes: Insight into role of vanadium in improving the photocatalytic activity

Harsha Bantawal[a], U. Sandhya Shenoy[b,*], D. Krishna Bhat[a,*]

[a] Department of Chemistry, National Institute of Technology Karnataka, Surathkal, Mangalore-575025, India
[b] Department of Chemistry, College of Engineering and Technology, Srinivas University, Mukka, Mangalore 574146, India

ARTICLE INFO

Keywords:
Photocatalysis
$SrTiO_3$
Vanadium doping
Electronic structure
Methylene blue

ABSTRACT

$SrTiO_3$ based materials have been gaining attention recently in the field of photocatalysis due to their tunable electronic structure. Herein, we employ a facile one pot solvothermal approach for the synthesis of V doped $SrTiO_3$ nanocubes. First principles theoretical calculations reveal that the 3 'd' dopant level introduced by V reduces the band gap and extends the absorption to the visible region of spectrum. The occupancy of Ti site by V introduces dopant states overlapping with the conduction band, eliminating the formation of mid gap recombination centres. Photocatalytic experimental studies on degradation of methylene blue dye reveals the material to be an excellent photocatalyst with high photocorrosion resistance and cyclic stability. In addition, the material is also predicted to be a potential thermoelectric material.

1. Introduction

Rising concern about environmental pollution due to the rapid pace of urbanization and industrialization has motivated the researchers towards the development of efficient and biocompatible photocatalysts. $SrTiO_3$, a perovskite material has been recently studied extensively due to its economic and environmentally friendly nature in the field of thermoelectrics, photocatalytic water splitting and degradation of organic pollutants [1–3]. For a material to be a good photocatalyst it should have an appropriate band gap, reduced recombination of charge carriers and resistance towards photocorrosion [4]. The large band gap of $SrTiO_3$ of about 3.2 eV makes it active only in the UV region and hence methods to reduce its band gap have been researched. Formation of nanocomposites and defect engineering are two useful approaches largely implemented to reduce the band gap and make $SrTiO_3$ photocatalytically active in visible region of solar spectrum [5–11]. Defects engineering involves either controlling the ratio of Sr/Ti/O or introduction of dopant atom into the host lattice [9–22]. Though the doping seems to be a favourable and easy approach in certain cases it is also known to introduce mid gap states acting as recombination centres thus countering the beneficial effect of reducing the band gap. Many dopants such as Ag, Al, Cr, F, Fe, La, Mo, Nb, Ni, Pt, Rh, Sb, Ta have been utilized to improve the photocatalytic activity of $SrTiO_3$ [3,12–21]. Co-doping has been implemented in certain cases to pacify the charge imbalance introduced by the aliovalent dopant [3,12,16,18,21]. But mainly these materials are used for photocatalytic hydrogen generation than degradation of organic pollutants. Hence, there is a requisite to find dopants which can have the beneficial effect of reducing the band gap while minimizing the formation of recombination centres.

Vanadium (V) doped in $SrTiO_3$ has been successfully studied for thermoelectric applications and photocatalytic water splitting application but has been hardly reported for photocatalytic degradation of organic dyes [18–22]. V being a transition element, has variable oxidation states. If it is introduced during doping with an aliovalent charge (say V^{3+} or V^{5+}) instead of isovalent charge (V^{4+}) from that of the atom which it is substituting (say Ti^{4+}) then there will be excess of charge in the doped sample. To compensate for the charge imbalance caused due to several such aliovalent substitutions, oxygen vacancies will be formed. The defect states introduced due to the formation of oxygen vacancies will act as recombination centres. Hence, there is a need to develop a synthetic route such that the dopant atom will be isovalent with that of the host atom which it is substituting. Herein, we report the study of V doped $SrTiO_3$ using both experimental and theoretical approach. We implement one pot facile solvothermal approach to synthesize the pristine as well as doped samples by avoiding high temperature calcination. The characterization reveals the successful doping of V^{4+} in $SrTiO_3$ and reduction in the band gap extending its absorption to visible region of the electromagnetic spectrum. Since, electronic structure of a material depends largely on the crystal

* Corresponding authors.
E-mail addresses: sandhyashenoy347@gmail.com (U.S. Shenoy), denthajekb@gmail.com (D.K. Bhat).

https://doi.org/10.1016/j.apsusc.2020.145858
Received 6 January 2020; Received in revised form 17 February 2020; Accepted 21 February 2020
Available online 21 February 2020

structure and site occupied by the dopant, we study the effect of site occupancy of V in $SrTiO_3$ [17,23,24]. The density functional theory (DFT) results reveal Ti site to be more favourable one for doping for photocatalytic applications, with bottom of the conduction band (CB) altered significantly as a result of doping. The photocatalytic activity of the material studied using methylene blue dye reveals it to be a potential material for environmental remediation.

2. Methods

2.1. Preparation of V-doped $SrTiO_3$

All the chemicals were purchased from Sigma-Aldrich and were used as received. Titanium (IV) isopropoxide (1.47 mL) was dissolved in 10 mL of 2-propanol. To this we added calculated amount of vanadyl acetylacetonate and stirred for one hour to ensure complete dissolution. An appropriate amount of strontium nitrate and 10 mL of 2 M KOH were added. The resultant mixture was sealed in an autoclave and kept in a hot air oven maintained at 200 °C for 4 h. The as obtained precipitates were washed thoroughly with acetic acid and water. The washed products were dried in an oven at 70 °C for 8 h. The products obtained by using 0.5, 1.0, 1.5 and 2.0 mol % of the V precursor were labelled as 0.5 V, 1.0 V, 1.5 V and 2.0 V respectively.

2.2. Characterization

We examined the phase and purity of the synthesized materials by using an X-ray diffractometer (XRD, Rigaku Miniflex 600) equipped with monochromatic Cu K_α radiation ($\lambda = 0.154$ nm) at a scan rate of 2° per minute in the 2θ range of 20°-80°. The surface morphology and nanostructure of the synthesized samples were analysed using field emission scanning electron microscopy (FESEM, Carl Zeiss Ultra 55), transmission electron microscopy (TEM) and high-resolution transmission electron microscopy (HRTEM, JEOL/JEM 2100). Kratos XSAM 800 spectrometer equipped with an Al K_α source was used to record X-ray photoelectron spectrum (XPS). We determined the specific surface area using the Brunauer-Emmett-Teller (BET) method (BEL SORP II, JAPAN). The pore size distribution was determined using the Barrett-Joyner-Halenda (BJH) method. The diffuse reflectance (DR) spectra were obtained using a UV–visible spectrometer (DRS, DR SPECORD S600 Analytic Jena). The photoluminescence (PL) spectra were recorded at room temperature (LS-55, PerkinElmer).

2.3. Determination of photocatalytic activity

To determine the photocatalytic activity, we used a photocatalytic reactor provided with a high-pressure 250 W Hg vapour lamp as a visible light source. Before photocatalytic studies, photocatalyst (50 mg) was dispersed in 100 mL of MB solution (10 mg L^{-1}) with the help of a sonicator for 5 min. We loaded the resultant solution into the reactor and then turned on the visible light source. 5 mL of the solution was sampled out periodically, centrifuged in order to separate the catalyst. The absorbance of the supernatant dye solution was measured using a UV–visible spectrometer at 664 nm. We calculated the percentage degradation of dye as per Eq. (1) [25].

$$\text{Degradation\%} = [(C_o - C)/C_o] \times 100 \quad (1)$$

where, C_o is the initial concentration of the dye solution and C is the concentration at different intervals of time.

2.4. Computational details

Using first principles DFT analysis, we investigated the electronic structure of $SrTiO_3$ and V doped $SrTiO_3$. Open source computer code Quantum ESPRESSO suite used for the study considered non-relativistic Martins-Troullier norm conserving pseudopotentials with local density approximation (Perdew-Wang functional type) to describe the electron wavefunctions [26,27]. We included 5 s^2, $3d^24s^2$, $2s^22p^4$, $4d^35s^1$ valence electrons of Sr, Ti, O and V, respectively in the simulations. $SrTiO_3$ crystallizes in cubic perovskite structure with Ti atom at the centre of the cube, O atoms at the face centre and Sr atoms at the corner. 2 × 2 × 2 supercell containing 40 atoms of primitive cell, were considered to simulate doped configurations. The plane wave basis representing the wavefunctions is truncated with 80 Ry of cut-off energy. A k mesh of 4 × 4 × 4 for self consistent field calculations and 8 × 8 × 8 for non-self consistent field calculations was made use of for the 2 × 2 × 2 supercell. Electronic structure was determined for fully relaxed supercells along Γ-X-M-Γ-R-X high symmetry points in the Brillouin zone.

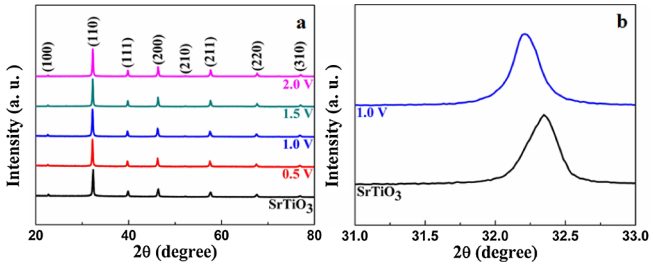

Fig. 1. (a) XRD patterns as a function of doping concentrations of V; (b) diffraction peaks of (1 1 0) planes in the range of 2θ = 31° − 33°.

3. Results and discussion

3.1. XRD analysis

We observe that the XRD patterns of $SrTiO_3$ and V-doped $SrTiO_3$ can be well matched with the standard perovskite phase of $SrTiO_3$ indexed in JCPDS card number 01-089-4934 (Fig. 1a). Successful incorporation of V in $SrTiO_3$ is revealed by the absence of impurity peaks in the XRD pattern. In Fig. 1b, we see that the (1 1 0) diffraction peaks of V-doped $SrTiO_3$ are slightly shifted towards lower 2θ values as V ions have smaller ionic radius than Sr or Ti ions. The shrinkage of lattice parameter of V doped $SrTiO_3$ samples is well documented and later also verified in theoretical section below [18,21].

3.2. TEM, EDS and BET surface area analysis

The TEM image of $SrTiO_3$ reveals irregular slightly elongated particles while that of 1.0 V sample reveals well formed nanocubes (Fig. 2a and b). EDS of 1.0 V indicates the presence of Sr, Ti, O and V (Fig. 2c). HRTEM analysis indicated uniform lattice fringes of about 2.78 Å which could be indexed to the (1 1 0) plane of $SrTiO_3$ (Fig. 2d). The BET surface area of the $SrTiO_3$ and 1.0 V were determined with the help of nitrogen adsorption-desorption isotherms. The nitrogen adsorption–desorption isotherms exhibited a type IV pattern with the hysteresis loops mimicking type H3 (in the P/P_o range of 0.4–1.0), indicating there may have been development of minute pores (Fig. 3) [28,29]. The higher BET surface area of the 1.0 V (36.3 m^2/g) in comparison to $SrTiO_3$ (26.45 m^2/g), facilitated the efficient adsorption and degradation of the pollutants by increasing the surface area and active site for catalysis, respectively. The pore size distribution of the 1.0 V sample was determined by BJH analysis. A broad pore size distribution can be seen in the inset of Fig. 3, which further indicates the presence of mesopores as well as macropores. The pore volume of 1.0 V was found to be 0.1381 cm^3/g which is almost three times that of $SrTiO_3$ (0.040 cm^3/g), promoting effective transport of reactants and products during the photocatalytic reaction.

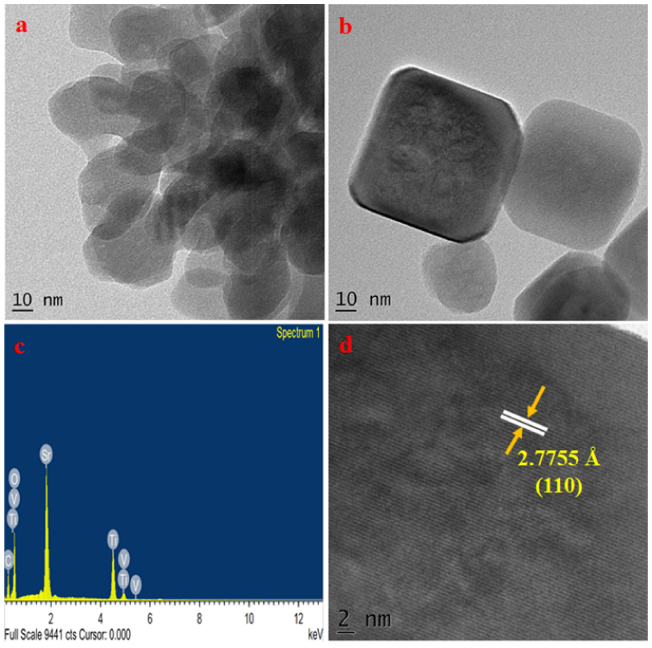

Fig. 2. TEM image of (a) $SrTiO_3$ and (b) 1.0 V; (c) EDS spectrum of 1.0 V; (d) HRTEM image of 1.0 V.

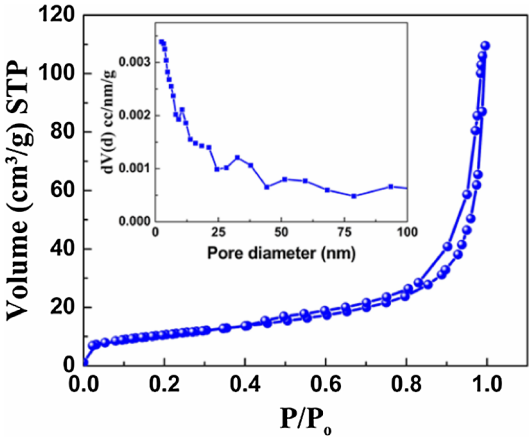

Fig. 3. Nitrogen adsorption-desorption isotherm and BJH pore size distribution (inset) of 1.0 V.

3.3. XPS analysis

XPS analysis indicated the presence of Sr, Ti, O in both $SrTiO_3$ and 1.0 V sample, while V only in the survey spectrum of 1.0 V sample. The peaks at binding energies 133.08 eV and 134.78 eV in the case of

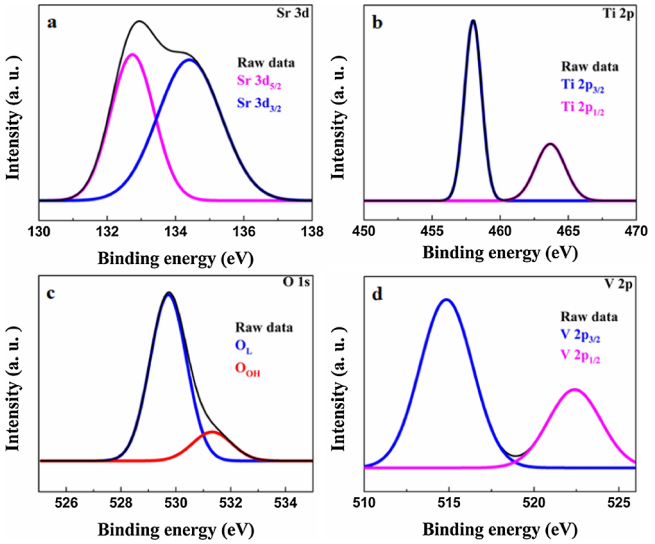

Fig. 5. High resolution XPS spectrum of 1.0 V (a) Sr 3d; (b) Ti 2p; (c) O 1s; (d) V 2p.

$SrTiO_3$ and 132.74 eV and 134.4 eV in the case of 1.0 V corresponds to Sr $3d_{5/2}$ and Sr $3d_{3/2}$ states, respectively (Fig. 4a and Fig. 5a) [30]. The peaks at binding energies 458.58 eV and 464.48 in $SrTiO_3$ and 457.9 eV and 463.67 eV in 1.0 V could be attributed to Ti $2p_{3/2}$ and Ti $2p_{1/2}$ states respectively indicating the oxidation state of Ti as + 4 (Fig. 4a and Fig. 5b) [30]. The binding energies of 529.82 eV and 531.04 for $SrTiO_3$ and 529.7 eV and 531.3 eV for 1.0 V could be allotted to lattice oxygen (O_L) and the surface hydroxyl groups (O_{OH}), respectively (Fig. 4c and Fig. 5c). The peaks at binding energies 515.2 eV and 523.2 eV could be ascribed to V $2p_{3/2}$ and V $2p_{1/2}$ states respectively implying the oxidation state of V as +4 (Fig. 5d) [31]. Since, V atoms were successfully doped into the Ti sites of $SrTiO_3$ in the V^{4+} oxidation state, thus avoiding the formation of oxygen vacancies which otherwise would have been created to maintain the charge neutrality. This indicates the effectiveness of the employed synthetic technique to minimize the formation of recombination centres. This is further confirmed by the PL studies.

3.4. Optical absorbance analysis

The DR spectra showed red shift in the absorption edge of V-doped $SrTiO_3$ in comparison to the pristine $SrTiO_3$ (Fig. 6a). This is attributed to the dopant level introduced by V as explained in the next section. The absorption data was derived using Kubelka-Munk equation (Eq. (2)) [32].

$$A/S = \frac{(1-R)^2}{2R} \quad (2)$$

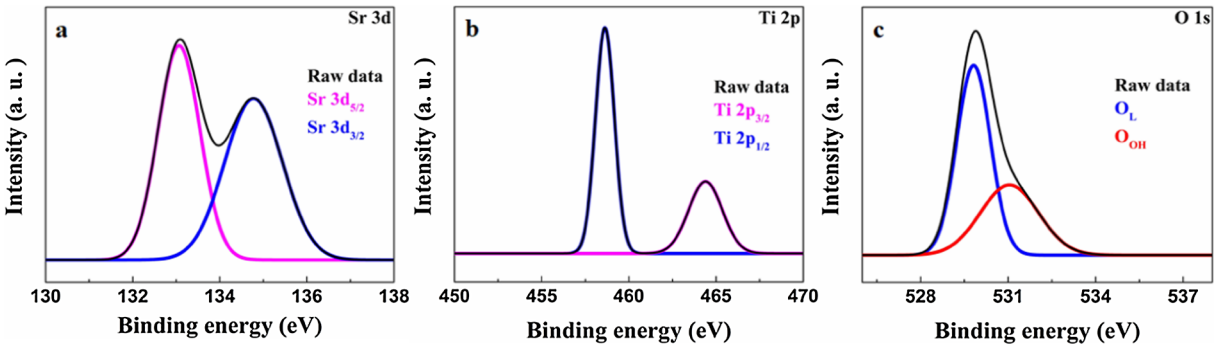

Fig. 4. High resolution XPS spectrum of $SrTiO_3$ (a) Sr 3d; (b) Ti 2p; (c) O 1s.

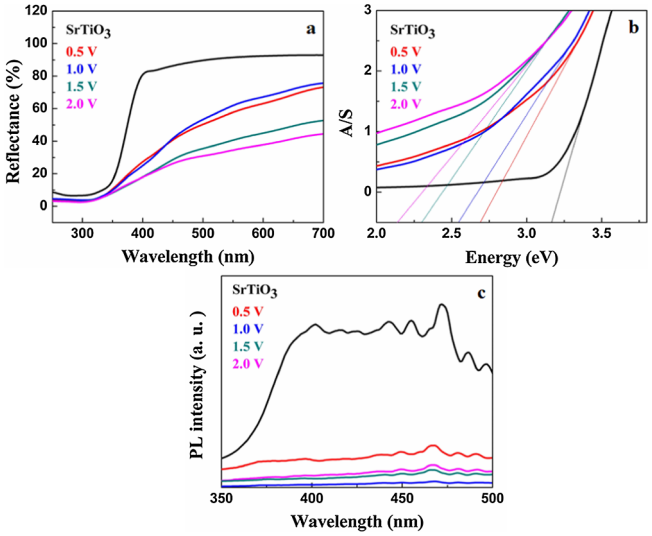

Fig. 6. (a) UV-visible DR spectra; (b) Electronic absorption spectra; (c) PL spectra of $SrTiO_3$ and V-doped $SrTiO_3$ samples.

where, R is the reflectance, A and S are the absorption and scattering coefficients. The band gap was determined by A/S versus energy plot (Fig. 6b) The band gaps of $SrTiO_3$, 0.5 V, 1.0 V, 1.5 V and 2.0 V were found to be 3.16 eV, 2.7 eV, 2.54 eV, 2.29 eV and 2.13 eV, respectively.

The PL intensity of V-doped $SrTiO_3$ is found to be extremely low in comparison to pristine $SrTiO_3$ indicating that V doped in 4 + oxidation state reduces the formation of the recombination centres and hence increases the charge carrier lifetime (Fig. 6c) [33,34]. 1.0 V shows the least PL intensity leading to the highest photocatalytic activity in degradation of MB as explained in the subsequent section. Aliovalent doping leads to introduction of oxygen vacancies to balance the charge. Since this synthetic technique introduces V in isovalent state as confirmed by XPS, the formation of oxygen vacancies is reduced thus reducing the chances of photo generated electron hole recombination.

3.5. Electronic structure analysis

The electronic structure of 2 × 2 × 2 supercell of the primitive $SrTiO_3$ revealed a direct band gap of 2.14 eV at Γ point (Fig. 7a). This is due to the R point of the Brillouin zone of primitive cell folding on to the Γ point of the supercell as previously reported [17]. The underestimation of band gap from the experimental value is typical of DFT based calculations due to the discontinuities present in the derivative of

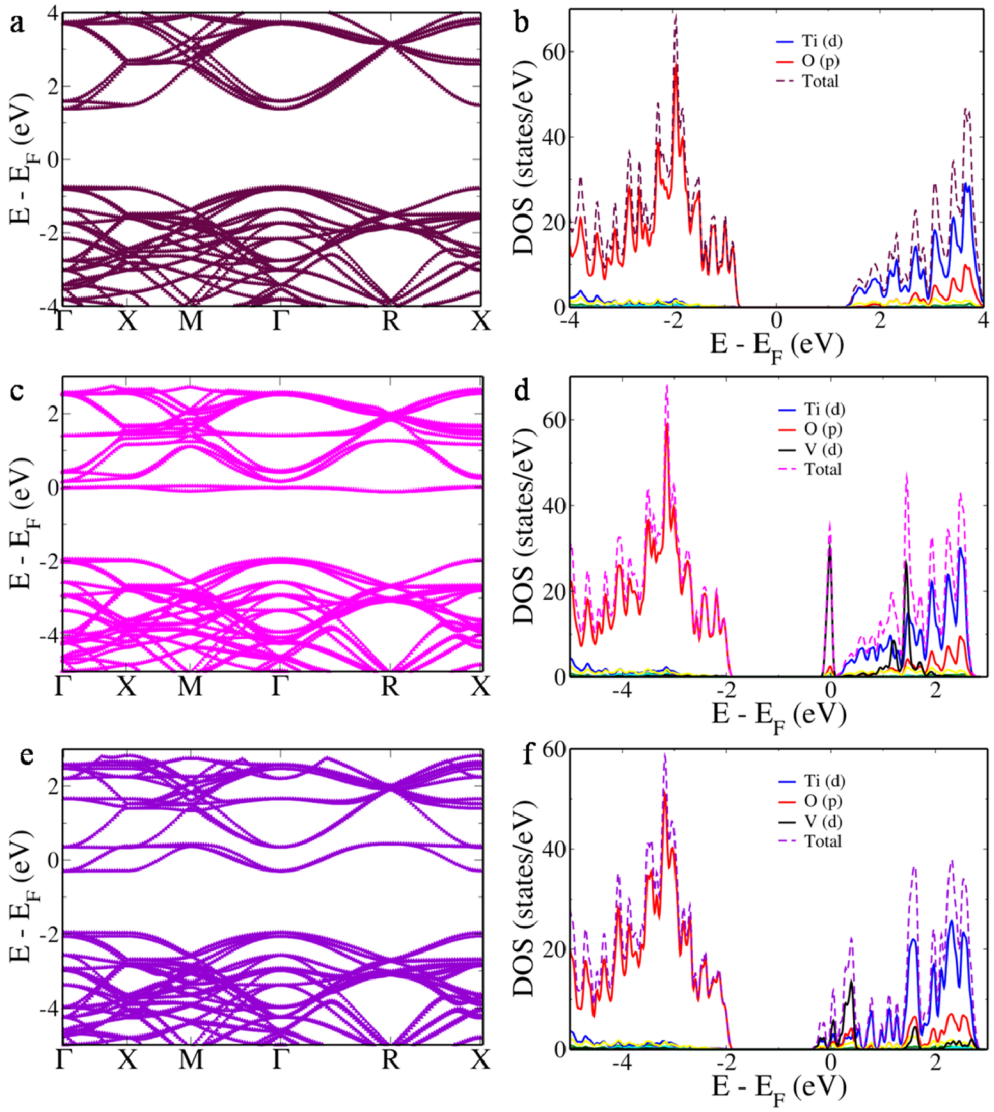

Fig. 7. Electronic structure and pDOS of pristine $SrTiO_3$ (a and b); V doped $SrTiO_3$ – V in Sr site (c and d); V doped $SrTiO_3$ – V in Ti site (e and f).

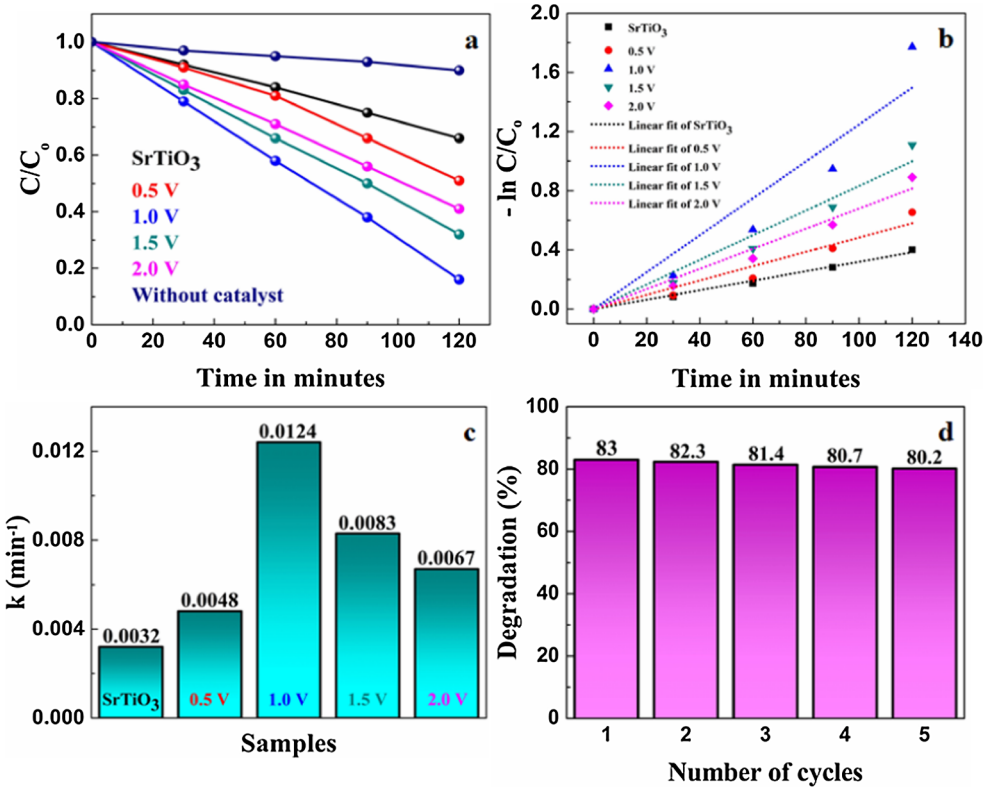

Fig. 8. (a) Photocatalytic MB degradation curves; (b) Pseudo first order kinetic plot of MB degradation; (c) Rate constants; (d) Cyclic stability of the synthesized 1.0 V.

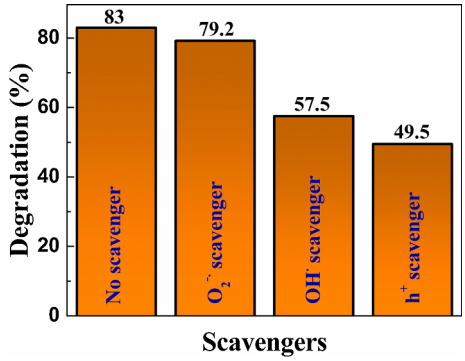

Fig. 9. Effect of radical scavengers on the photocatalytic degradation of MB by 1.0 V.

energy with respect to number of electrons [32]. The density of states (DOS) was projected on to the atomic orbitals of Sr, Ti and O atoms (Fig. 7b). *p* orbitals of O forms the valence band (VB). *d* orbitals of Ti with little contribution from *p* orbitals of O forms the conduction band (CB) states. The Sr atoms do not contribute to VB or CB which completely agrees with the fully ionic character of Sr. As doping of V can introduce V into Sr site or Ti site, we carried out simulations for both the cases at various doping concentrations. When V substitutes for Sr, the lattice constant estimated is 3.804 Å, smaller than the lattice constant of 3.808 Å estimated for V substituting Ti. The bond lengths of V to O decreases by 0.03 Å compared to Ti-O and Sr-O bonds due to the smaller ionic radius of V. While, the V-Ti bond (when V is in Sr site) measures about 3.284 Å, the Sr-Ti and Sr-V bond measures 3.302 Å and 3.300 Å, respectively. When V occupies Sr site the direct band gap at Γ point decreases to 1.93 eV (Fig. 7c). The projected density of states (pDOS) reveals that the decrease in the band gap is due to the appearance of a defect level just beneath the CB constituted by *d* orbitals of V. Around 1.5 eV into the conduction band we see hybridization of V and Ti *d* orbitals appearing as another sharp peak. The rest of the features remains the same as that of the pristine $SrTiO_3$ (Fig. 7d). The flat nature of the defect band just beneath the CB points towards the photocorrosion resistance of the material predicting it to be highly stable photocatalyst [35,36]. In addition to it, the distortion in the DOS at the Fermi level with the appearance of very sharp peak predicts V to be a resonant dopant in $SrTiO_3$ like recently reported Bi or Zn in SnTe [37,38].

We see that when V occupies Ti site the direct band gap further decreases to 1.66 eV (Fig. 7e). The pDOS reveals the mixing of *d* orbitals of V and Ti at the CB edge forming a continuous band extending downwards decreasing the band gap while *p* orbitals of O forms the VB as in the case of undoped material (Fig. 7f). The contribution of V is found to be more spread out in the case of Ti site than in Sr site. The continuous nature of the band structure at the CB as revealed by pDOS plot facilitates easy migration of photogenerated carriers avoiding the dopant states from becoming trap centres there by increasing the efficiency [17,39].

3.6. Photocatalytic activity

The photocatalytic efficiency of the synthesized materials was evaluated for the decomposition of MB dye solution under visible light (Fig. 8a). In the absence of catalyst there is no appreciable degradation of MB. We observe that the photocatalytic activity of V doped $SrTiO_3$ samples is higher than the pristine $SrTiO_3$. This is attributed to the decrease in the band gap of the material with increase in the dopant concentration. Substitution of V in Ti site introduces continuous energy level in CB facilitating the easy migration and separation of photogenerated charge carriers. In addition to it 1.0 V sample shows higher surface area facilitating higher absorption of MB dyes leading to subsequent degradation of adsorbed molecules.

The kinetics of the photocatalytic degradation of MB by $SrTiO_3$ and V-doped $SrTiO_3$ is in good agreement with the pseudo first-order rate

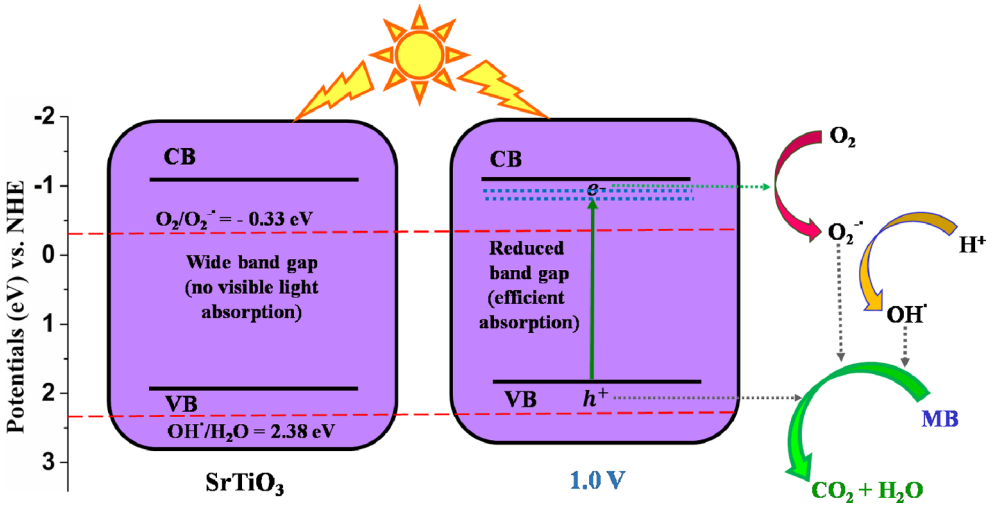

Fig. 10. The photocatalytic mechanism for the degradation of MB by V doped $SrTiO_3$ under visible light irradiation.

Table 1
Thermodynamic parameters of $SrTiO_3$ and V doped $SrTiO_3$ samples.

Sample	E_a (kJ/mol)	$\Delta H^{\#}$ (kJ/mol)	$\Delta S^{\#}$ (kJ/mol)	$\Delta G^{\#}$ (kJ/mol)
$SrTiO_3$	14.3	11.8	−0.25	87.8
0.5 V	13.3	10.8	−0.25	86.8
1.0 V	10.9	8.4	−0.25	84.4
1.5 V	11.9	9.4	−0.25	85.4
2.0 V	12.4	9.9	−0.25	85.9
Without catalyst	17.7	15.2	−0.25	91.2

equation given by (3) [40].

$$-\ln(C/C_o) = kt \quad (3)$$

where, C_o is the initial concentration of dye, C is the concentration of the dye at irradiation time (t) and k is the first order rate constant. k in turn is calculated from the slope of the straight line plot of $-\ln(C/C_o)$ versus t (Fig. 8b). The rate constant of 1.0 V was found to be higher than all the other samples indicating the high efficiency of the sample (Fig. 8c). The high stability of 1.0 V is further confirmed from the cyclic stability test indicating the photocorrosion resistance as revealed by the electronic structure studies (Fig. 8d) [41].

Trapping experiments were carried out in order to determine the active species involved in the photocatalytic degradation. The procedure followed was similar to the one used for degradation measurements as above but with the addition of different radical scavenging agents like benzoquinone (1 mM) as a superoxide anion radical ($O_2^{-\cdot}$) scavenger, potassium iodide (10 mM) as a hole (h^+) scavenger and isopropyl alcohol (10 mM) as a hydroxyl radical ($OH^{\cdot}$) scavenger (Fig. 9) [42]. We see that superoxide radical anions are not the major active species as the corresponding scavenger benzoquinone did not deteriorate the photocatalytic activity much. Whereas the addition of potassium iodide (hole scavenger) and isopropyl alcohol ($OH^{\cdot}$ scavenger) reduced the photocatalytic activity significantly. As a result, holes followed by hydroxyl radicals are considered to be the active species for the effectual degradation of dye.

We propose the mechanism of degradation as follows: When V doped $SrTiO_3$ is irradiated with an energy equal to or greater than its band gap, electrons from the VB get excited to the CB leaving corresponding number of holes in VB. These electrons in CB react with oxygen to produce superoxide radicals ($O_2^{-\cdot}$). Some of these later react with the protons present to form hydroxyl radicals ($OH^{\cdot}$). The holes in VB directly react with MB. The formed radicals are said to be active species for the effectual degradation of MB to CO_2 and water (Fig. 10).

The activation energy for the photocatalytic degradation of MB can be calculated by using the Eq. (4) [43,44].

$$\log\ k = \frac{-E_a}{2.303RT} \quad (4)$$

where, k is the rate constant of photocatalytic degradation, E_a is the energy of activation, R is the gas constant (R = 8.314 J/K) and T is the temperature in kelvin (K) scale taken as 300 K in the current study.

The other thermodynamic parameters such as, free energy of activation ($\Delta G^{\#}$), enthalpy of activation ($\Delta H^{\#}$) and entropy of activation ($\Delta S^{\#}$) were computed by employing activated complex theory (ACT) and Eyring equation as given below (Table 1).

$$\ln\ k = \ln(k_B T/h) - \Delta H^{\#}/RT + \Delta S^{\#}/R \quad (5)$$

$$\Delta H^{\#} = E_a - RT \quad (6)$$

$$\Delta G^{\#} = \Delta H^{\#} - T\Delta S^{\#} \quad (7)$$

where, k_B is the Boltzmann's constant (1.3805×10^{-23} J/K) and h is the Planck's constant (6.6261×10^{-34}Js).

From the values tabulated we observe that higher energy of activation is required for the photodegradation of MB without catalyst whereas relatively lower energy of activation is needed in presence of $SrTiO_3$ and V doped $SrTiO_3$. This ascertains that the catalyst alters the path of the reaction by lowering activation energy. 1.0 V sample exhibited lowest activation energy as compared to other samples. The endothermic and non spontaneous nature of the reaction was revealed by the positive enthalpy and free energy change.

4. Conclusions

V doped $SrTiO_3$ nanocubes was successfully synthesized by a facile one pot solvothermal approach which incorporated V^{4+} ions into Ti sites of $SrTiO_3$. The band gap of the doped samples decreased due to the formation of dopant levels just beneath the CB as predicted by the DFT calculations. The isovalent doping prevents the formation of recombination centres increasing the photocatalytic activity along with the increased surface area of the nanocubes. The high photocatalytic activity of MB degradation and stability of V doped $SrTiO_3$ (1.0 V) indicates that the material can be potentially used for environmental remediation for degradation of organic pollutants.

Declaration of Competing Interest

The authors declare that they have no known competing financial interests or personal relationships that could have appeared to influence the work reported in this paper.

References

[1] A.V. Kovalevsky, M.H. Aguirre, S. Populoh, S.G. Patrício, N.M. Ferreira, S.M. Mikhalev, D.P. Fagg, A. Weidenkaff, J.R. Frade, Designing strontium titanate-based thermoelectrics: insight into defect chemistry mechanisms, J. Mater. Chem. A 5 (2017) 3909–3922.

[2] B.L. Phoon, C.W. Lai, J.C. Juan, P.L. Show, G.T. Pan, Recent developments of strontium titanate for photocatalytic water splitting application, Int. J. Hydrog. Energy 44 (2019) 14316–14340.

[3] J. Jiang, Y. Jia, Y. Wang, R. Chong, L. Xu, X. Liu, Insight into efficient photocatalytic elimination of tetracycline over $SrTiO_3$ (La, Cr) under visible-light irradiation: The relationship of doping and performance, Appl. Surf. Sci. 486 (2019) 93–101.

[4] M.M.J. Sadiq, U.S. Shenoy, D.K. Bhat, Synthesis of $BaWO_4$/NRGO–g-C_3N_4 nanocomposites with excellent multifunctional catalytic performance via microwave approach, Front. Mater. Sci. 12 (2018) 247–263.

[5] J. Zwara, M. Paszkiewicz-Gawron, J. Łuczak, A. Pancielejko, W. Lisowski, G. Trykowski, A. Zaleska-Medynska, E. Grabowska, The effect of imidazolium ionic liquid on the morphology of Pt nanoparticles deposited on the surface of $SrTiO_3$ and photoactivity of Pt–$SrTiO_3$ composite in the H_2 generation reaction, Int. J. Hydrog. Energy 44 (2019) 26308–26321.

[6] B. Thomas, L.K. Alexander, Nanoreactor based enhancement of photocatalysis with $Co_{0.7}Zn_{0.3}Fe_2O_4$@$SrTiO_3$ core-shell nanocomposites, J. Alloys Compd. 788 (2019) 257–266.

[7] C.W. Chang, C. Hu, Graphene oxide-derived carbon-doped $SrTiO_3$ for highly efficient photocatalytic degradation of organic pollutants under visible light irradiation, Chem. Eng. J. 123116 (2019), https://doi.org/10.1016/j.cej.2019.123116.

[8] H. Bantawal, M. Sethi, U.S. Shenoy, D.K. Bhat, Porous graphene wrapped $SrTiO_3$ nanocomposite: Sr–C Bond as an effective coadjutant for high performance photocatalytic degradation of methylene blue, ACS Appl. Nano Mater. 2 (2019) 6629–6636.

[9] X. Ma, Z. Wu, E.J. Roberts, R. Han, G. Rao, Z. Zhao, M. Lamoth, X. Cui, R.D. Britt, F.E. Osterloh, Surface photovoltage spectroscopy observes sub-band-gap defects in hydrothermally synthesized $SrTiO_3$ nanocrystals, J. Phys. Chem. C 123 (2019) 25081–25090.

[10] K. Yamada, H. Suzuki, R. Abe, A. Saeki, Complex photoconductivity reveals how the nonstoichiometric Sr/Ti affects the charge dynamics of a $SrTiO_3$ photocatalyst, J. Phys. Chem. Lett. 10 (2019) 1986–1991.

[11] H. Bantawal, U.S. Shenoy, D.K. Bhat, Tuning the photocatalytic activity of $SrTiO_3$ by varying the Sr/Ti ratio: unusual effect of viscosity of the synthesis medium, J. Phys. Chem. C 122 (2018) 20027–20033.

[12] Y. Yu, Z. Lu, Q. Guo, J. Yu, Y. Li, X. Zhang, Y. Cheng, Y. Yao, H. Liu, Enhanced solar-light-driven photocatalytic performance by the synergistic effects of F− doped and Ag loaded $SrTiO_3$ cubic nanoparticles, Chem. Phys. Lett. 692 (2018) 94–101.

[13] Z. Zhao, R.V. Goncalves, S.K. Barman, E.J. Willard, E. Byle, R. Perry, Z. Wu, M.N. Huda, A.J. Moulé, F.E. Osterloh, Electronic structure basis for enhanced overall water splitting photocatalysis with aluminum doped $SrTiO_3$ in natural sunlight, Energy Environ. Sci. 12 (2019) 1385–1395.

[14] A. Mikuła, E. Drożdż, A. Koleżyński, Electronic structure and structural properties of Cr-doped SrTiO3–Theoretical investigation, J. Alloys Compd. 749 (2018) 931–938.

[15] Y. Hu, G. Zhao, Q. Pan, H. Wang, Z. Shen, B. Peng, G.W. Busser, X. Wang, M. Muhler, Highly selective anaerobic oxidation of alcohols over Fe-doped $SrTiO_3$ under visible light, Chem. Cat. Chem 11 (2019) 5139–5144.

[16] Y. Yamaguchi, S. Usuki, K. Yamatoya, N. Suzuki, K.I. Katsumata, C. Terashima, A. Fujishima, A. Kudo, K. Nakata, Efficient photocatalytic degradation of gaseous acetaldehyde over ground Rh–Sb co-doped $SrTiO_3$ under visible light irradiation, RSC Adv. 8 (2018) 5331–5337.

[17] U.S. Shenoy, H. Bantawal, D.K. Bhat, Band engineering of $SrTiO_3$: effect of synthetic technique and site occupancy of doped rhodium, J. Phys. Chem. C 122 (2018) 27567–27574.

[18] B. Modak, S.K. Ghosh, Insight into the enhanced photocatalytic activity of $SrTiO_3$ in the presence of a (Ni, V/Nb/Ta/Sb) pair, Phys. Chem. Chem. Phys. 20 (2018) 20078–20087.

[19] J.D. Baniecki, M. Ishii, H. Aso, K. Kurihara, D. Ricinschi, Density functional theory and experimental study of the electronic structure and transport properties of La, V, Nb, and Ta doped $SrTiO_3$, J. Appl. Phys. 113 (2013) 013701.

[20] C.S. Park, M.H. Hong, H.H. Cho, H.H. Park, Enhancement of Seebeck coefficient of mesoporous $SrTiO_3$ with V-group elements V, Nb, and Ta substituted for Ti, J. Eur. Ceram. Soc. 38 (2018) 125–130.

[21] V.Q.T. Hoang, T.Q.P. Phan, V. Senthilkumar, V.T. Doan, Y.S. Kim, M.V. Le, Enhanced photocatalytic activities of vandium and molybdenum co-doped strontium titanate under visible light, Int. J. Appl. Ceram. Technol. 16 (2019) 1651–1658.

[22] C. Adessi, S. Thébaud, G. Bouzerar, Ab initio investigation of the role of vanadium impurity states in $SrTiO_3$ for thermoelectricity, J. Phys. Chem. Solids 138 (2019) 109180.

[23] D.K. Bhat, U.S. Shenoy, High thermoelectric performance of co-doped tin telluride due to synergistic effect of magnesium and indium, J. Phys. Chem. C 121 (2017) 7123–7130.

[24] X. Xu, H. Jiang, First-principles investigation on anion order, electronic structure and dielectric properties of $BaTaO_2N$, J. Mater. Chem. A 7 (2019) 14583–14591.

[25] M.M.J. Sadiq, U.S. Shenoy, D.K. Bhat, $NiWO_4$-ZnO-NRGO ternary nanocomposite as an efficient photocatalyst for degradation of methylene blue and reduction of 4-nitro phenol, J. Phys. Chem. Solids 109 (2017) 124–133.

[26] P. Giannozzi, S. Baroni, N. Bonini, M. Calandra, R. Car, C. Cavazzoni, D. Ceresoli, G.L. Chiarotti, M. Cococcioni, I. Dabo, A. Dal Corso, S. de. Gironcoli, S. Fabris, G. Fratesi, R. Gebauer, U. Gerstmann, C. Gougoussis, A. Kokalj, M. Lazzeri, L. Martin-Samos, N. Marzari, F. Mauri, R. Mazzarello, S. Paolini, A. Pasquarello, L. Paulatto, C. Sbraccia, S. Scandolo, G. Sclauzero, A.P. Seitsonen, A. Smogunov, P. Umari, R.M. Wentzcovitch, QUANTUM ESPRESSO: a modular and open-source software project for quantum simulations of materials, J. Phys.: Condens. Matter 21 (2009) 395502.

[27] J.P. Perdew, K. Burke, M. Ernzerhof, Generalized gradient approximation made simple, Phys. Rev. Lett. 77 (1996) 3865.

[28] M. Sethi, H. Bantawal, U.S. Shenoy, D.K. Bhat, Eco-friendly synthesis of porous graphene and its utilization as high performance supercapacitor electrode material, J. Alloys Compd. 799 (2019) 256–266.

[29] M. Sethi, U.S. Shenoy, D.K. Bhat, Porous graphene-$NiCo_2O_4$ nanorod hybrid composite as high performance supercapacitor electrode material, New J. Chem. (2020), https://doi.org/10.1039/C9NJ05725K.

[30] Z. Wu, Y. Zhang, X. Wang, Z. Zou, Ag@ $SrTiO_3$ nanocomposite for super photocatalytic degradation of organic dye and catalytic reduction of 4-nitrophenol, New J. Chem. 41 (2017) 5678–5687.

[31] J. Macías, A.A. Yaremchenko, E. Rodríguez-Castellón, M. Starykevich, J.R. Frade, Compromising between phase stability and electrical performance: $SrVO_3$–$SrTiO_3$ solid solutions as solid oxide fuel cell anode components, Chem. Sus. Chem 12 (2019) 240–251.

[32] D.K. Bhat, U.S. Shenoy, Zn: A versatile resonant dopant for SnTe thermoelectrics, Mater. Today Phys. 100158 (2019), https://doi.org/10.1016/j.mtphys.2019.100158.

[33] M.M.J. Sadiq, U.S. Shenoy, D.K. Bhat, Novel RGO–$ZnWO_4$–Fe_3O_4 nanocomposite as high performance visible light photocatalyst, RSC Adv. 6 (2016) 61821–61829.

[34] D. Yang, X. Zhao, X. Zou, Z. Zhou, Z. Jiang, Removing Cr (VI) in water via visible-light photocatalytic reduction over Cr-doped $SrTiO_3$ nanoplates, Chemosphere 215 (2019) 586–595.

[35] A. Roy, U.S. Shenoy, K. Manjunath, P. Vishnoi, U.V. Waghmare, C.N.R. Rao, Structure and properties of $Cd_4P_2Cl_3$, an analogue of CdS, J. Phys. Chem. C 120 (2016) 15063–15069.

[36] S. Shenoy, U.V. Waghmare, S.R. Lingampalli, A. Roy, C.N.R. Rao, Effects of alio-valent anion substitution on the electronic structures and properties of ZnO and CdS, Isr. J. Chem. 57 (2017) 477–489.

[37] U.S. Shenoy, D.K. Bhat, Electronic structure engineering of tin telluride through co-doping of bismuth and indium for high performance thermoelectrics: a synergistic effect leading to a record high room temperature ZT in tin telluride, J. Mater. Chem. C 7 (2019) 4817–4821.

[38] U.S. Shenoy, D.K. Bhat, Bi and Zn co-doped SnTe thermoelectrics: interplay of resonance levels and heavy hole band dominance leading to enhanced performance and record high room temperature ZT, J. Mater. Chem. C 8 (2020) 2036–2042.

[39] H.C. Chen, C.W. Huang, J.C. Wu, S.T. Lin, Theoretical investigation of the metal-doped $SrTiO_3$ photocatalysts for water splitting, J. Phys. Chem. C 116 (2012) 7897–7903.

[40] M.J.S. Mohamed, U.S. Shenoy, D.K. Bhat, High performance dual catalytic activity of novel zinc tungstate-reduced graphene oxide nanocomposites, Adv. Sci. Eng. Med. 9 (2017) 115–121.

[41] A.C. Nogueira, L.E. Gomes, J.A. Ferencz, J.E. Rodrigues, R.V. Gonçalves, H. Wender, Improved visible light photoactivity of $CuBi_2O_4$/CuO heterojunctions for photodegradation of methylene blue and metronidazole, J. Phys. Chem. C 123 (2019) 25680–25690.

[42] M.M.J. Sadiq, U.S. Shenoy, D.K. Bhat, Enhanced photocatalytic performance of N-doped RGO-$FeWO_4$/Fe_3O_4 ternary nanocomposite in environmental applications, Mater. Today Chem. 4 (2017) 133–141.

[43] A.S. Kshirsagar, P.K. Khanna, $CuSbSe_2$/TiO_2: novel type-II heterojunction nano-photocatalyst, Mater. Chem. Front. 3 (2019) 437–449.

[44] D.P. Jaihindh, A. Verma, C.C. Chen, Y.C. Huang, C.L. Dong, Y.P. Fu, Study of oxidation states of Fe-and Co-doped TiO_2 photocatalytic energy materials and their visible-light-driven photocatalytic behavior, Int. J. Hydrog. Energy 44 (2019) 15892–15906.